Reflection and Emission Models for Deserts Derived from Nimbus-7 ERB Scanner Measurements

W. FRANK STAYLOR AND JOHN T. SUTTLES

Atmospheric Sciences Division, NASA Langley Research Center, Hampton, VA 23665

(Manuscript received 15 February 1985, in final form 12 August 1985)

ABSTRACT

Broadband shortwave and longwave radiance measurements obtained from the Nimbus-7 Earth Radiation Budget scanner were used to develop reflectance and emittance models for the Sahara–Arabian, Gibson, and Saudi Deserts. The models were established by fitting the satellite measurements to analytic functions. For the shortwave, the model function is based on an approximate solution to the radiative transfer equation. The bidirectional-reflectance function was obtained from a single-scattering approximation with a Rayleigh-like phase function. The directional-reflectance model followed from integration of the bidirectional model and is a function of the sum and product of cosine solar and viewing zenith angles, thus satisfying reciprocity between these angles. The emittance model was based on a simple power-law of cosine viewing zenith angle.

1. Introduction

Deserts and arid regions form a substantial portion of the Earth's land area and must be treated as a major surface type in radiation budget studies. Deserts basically differ from other surface types in that they have high albedos as well as high thermal emissions. Therefore, increased desertification in the equatorial regions of Africa, Asia, and South America could alter the existing radiation balance in ways that might produce significant climate changes (Bryson and Baerreis, 1967). Also, many deserts are large, stable and uniform, have high albedos and clear skies, and generally provide ideal natural targets for long-term, inflight calibration of satellite radiometers. For all of these reasons, reflection and emission models are needed that can characterize the radiative properties of deserts.

A cloud-free dataset of broadband shortwave and longwave radiance measurements of the Sahara–Arabian Desert taken by the Nimbus-7 Earth Radiation Budget (ERB) scanner was compiled and processed into statistical parameters at NOAA/NESDIS (Taylor et al., 1983; Taylor and Stowe, 1984). The multi-axis scanning capability of the ERB scanner provided measurements over a wide range of angular parameters which are particularly useful for modeling purposes. In the present paper, this large Sahara–Arabian Desert dataset was used to develop basic reflection and emission models for deserts. The general applicability of these models was assessed from limited ERB datasets for the Gibson Desert, which is darker and somewhat less arid, and the Saudi Desert which is brighter and somewhat more arid than the Sahara–Arabian Desert.

2. Satellite measurements

a. Satellite and instruments

The Nimbus-7 satellite was launched 24 October 1978, into a noon, Sun-synchronous orbit to an altitude of 950 km and inclination of 99°. The ERB scanner had four telescopes, each of which had a broadband shortwave (0.2–4 μm) and longwave (5–50 μm) channel. It scanned from horizon-to-horizon along the orbital groundtrack and to a zenith angle of 72° in the crosstrack direction. At the nadir, the spatial resolution was about 90 km which increased to about 250 km at the horizon. A more detailed description of the ERB instrument and its operation is given by Jacobowitz et al. (1984).

b. Datasets

The dataset used to develop the basic reflection and emission models for deserts consisted of 123 141 pairs of shortwave, L_{SW}, and longwave, L_{LW}, radiances from the Sahara–Arabian Desert measured by the Nimbus-7 ERB scanner during the period from November 1978 to May 1980 (Stowe and Fromm, 1983). These data were sorted into 196 ranges of angles, called bins, in order to provide discrete parameter values for modeling and display. Bins were sorted by viewing zenith angle, θ, azimuth angle, ϕ ($\phi = 0°$, forward reflection; $\phi = 180°$, backward reflection), and $U_0 = \cos\theta_0$ where θ_0 is the solar zenith angle. Bin angular ranges are given in Table 1. For each of the data bins, the bin description ($\theta - \phi - U_0$), mean of both L_{SW}/U_0 and L_{LW}, and the bin population were available in tabular form. In ad-

TABLE 1. Sahara–Arabian data bins.

θ Range (deg)	ϕ Range* (deg)	θ_0 Range (U_0)	θ_0 Range (deg)
0–15**	0–9	1.0–0.9	0–26
15–27	9–30	0.9–0.8	26–37
27–39	30–60	0.8–0.7	37–46
39–51	60–90	0.7–0.6	46–53
51–63	90–120		
63–75	120–150		
75–90	150–171		
	171–180		

* Assumed symmetry about principal plane
** Single cap bin

dition, the albedo, A, was computed for each of the four U_0 ranges using a mean Earth–Sun distance solar flux of $S_0 = 1376$ W m^{-2}.

The Nimbus-7 ERB data used to model the Gibson and Saudi Deserts were taken during several days in December 1978 and March, July and December 1979. These measurements were individual shortwave and longwave radiance pairs (i.e., not binned) obtained from master archive tapes (Jacobowitz et al., 1984) archived at the Langley Research Center. The December 1978 through July 1979 data provided maximum, medium, and minimum solar zenith angles at both sites, and the December 1979 data were added for direct comparisons with the December 1978 data to determine whether sensor degradations had occurred during the year. Dataset populations and angular ranges are given in Table 2.

Measurements having clouds within the instantaneous field-of-view of the ERB scanner were eliminated from the Sahara–Arabian dataset using the Temperature-Humidity Infrared Radiometer (THIR, also onboard Nimbus 7) window channel (11 μm) in an editing technique developed by Stowe (1983). Cloudy days were eliminated from the Gibson and Saudi datasets by analyzing the general levels of the ERB L_{SW} and L_{LW} values (overcast) and by requiring continuity in the daily plots of L_{LW} versus θ (partial cloudiness).

3. Description of desert sites

The Sahara–Arabian Desert covers the majority of northern Africa and the Arabian Peninsula and is by far the largest desert on our planet. It can generally be characterized as having vast expanses of sand dunes, sand seas, arid gravel, and rock outcroppings with little moisture or vegetation (Short et al., 1976). The boundaries for the Sahara–Arabian dataset were 15°N to 30°N latitude, 15°W to 50°E longitude, and all cloud-free desert measurements within these borders were included in the dataset. Although the desert is not uniform for this large area, each data bin contains measurements from over the entire area, and the averaged bin dataset treats the Sahara–Arabian as though it were a uniform desert.

The Gibson Desert site is located in western Australia and is bounded by latitudes 25.0°S to 27.5°S and longitudes 120.0°E to 122.5°E. This site has a mixture of sand dunes, dry salt lakes, rock outcroppings, and arid steppe vegetation. The Saudi Desert site is located in the Ar Rab Al Khali basin of the Arabian Peninsula and is bounded by latitudes 20.0°N to 22.5°N and longitudes 50.0°E to 52.5°E. This general area is often referred to as the Arabian Empty Quarter, but because it is located totally within the borders of Saudi Arabia, it will be referred to here as the Saudi Desert. This site is almost entirely sand dunes and sand seas, and the lack of moisture and saline nature of the sand cause it to be virtually free of all vegetation (Short et al., 1976). Unpublished Nimbus-6 ERB data indicated that both of these relatively small desert sites were uniform (±5%), and that the Gibson site was darker and the Saudi site was brighter than the overall Sahara–Arabian Desert.

4. Reflected shortwave

a. *Sahara–Arabian bidirectional model*

Bidirectional reflectance is defined here as

$$R = \frac{\pi L_{SW}}{SU_0} \tag{1}$$

which is a function of θ_0, θ and ϕ (S is the distance-corrected solar flux). An azimuthally independent reflectance is defined as

$$\bar{R} = \frac{1}{2\pi}\int_0^{2\pi} R d\phi. \tag{2}$$

Barkstrom (1973), using single-scattering approximations, found that $\bar{R}UU_0$ could be expressed as a function of $UU_0/(U + U_0)$ where $U = \cos\theta$. Staylor (1985) also found these parameters to be useful for the directional modeling of overcast low, middle, and high water clouds and high ice clouds.

Reflectance parameters, $\bar{R}UU_0$, for the Sahara–Arabian Desert data are presented in Fig. 1 as a function of $UU_0/(U + U_0)$. The data are well correlated along a curve related by the equation

TABLE 2. Dataset ranges and population.

Desert site	θ (deg)	ϕ (deg)	θ_0 (deg)	Measurements
Sahara–Arabian	6–87	0–360	0–53	191 bins*
Gibson	18–85	5–336	4–50	63 points
Saudi	6–86	2–356	4–47	62 points

* Five of 196 potential bins had insufficient data

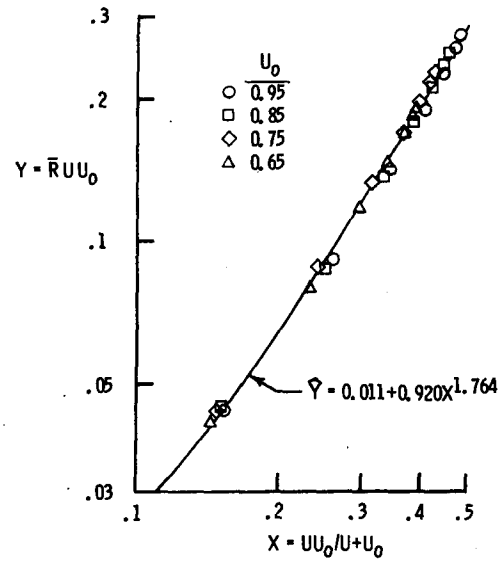

FIG. 1. Correlation of the directional reflectance for the Sahara–Arabian Desert as a function of viewing and solar zenith angles.

$$Y = Y_0 + Y_1 X^N \tag{3}$$

where $X = UU_0/(U + U_0)$ and $Y = \bar{R}UU_0$. A general discussion of the technical significance of the regression coefficients Y_0, Y_1, and N is given by Staylor (1985).

b. Azimuthal phase function

The parameter $\bar{R}$ is useful for correlative purposes and for the calculation of albedo. However, in many instances, insufficient azimuth angle data are available to compute this parameter accurately. This is the case for the Gibson and Saudi datasets where an azimuthal phase function is needed that will convert the measured R values into $\bar{R}$ values. The azimuthally-binned, Sahara–Arabian dataset was ideally suited for determining the general form of this function.

Staylor (1985) found that the bidirectional reflectances for clouds were well correlated with scattering angle, γ, which can be expressed as

$$\cos\gamma = \sin\theta \sin\theta_0 \cos\phi - \cos\theta \cos\theta_0 \tag{4}$$

where $\gamma = 0°$ is forward scattering and $\gamma = 180°$ is backward scattering. Plots of R versus γ for constant bin values of θ and θ_0 indicated that the Sahara–Arabian reflectances behaved in a Rayleigh-like manner and could be approximated as

$$R = R_{MIN}(1 + C_{SW} \cos^2\gamma) \tag{5}$$

where R_{MIN} was a function of θ and θ_0 and C_{SW} was a constant. Thus, an azimuthal phase function, P_{SW}, can be expressed as

$$P_{SW} = \frac{R}{\bar{R}} = \frac{1 + C_{SW}[UU_0 - VV_0 \cos\phi]^2}{1 + C_{SW}[(UU_0)^2 + \frac{1}{2}(VV_0)^2]} \tag{6}$$

where $V = \sin\theta$ and $V_0 = \sin\theta_0$. A least squares regression fit of $Y = RUU_0/P_{SW}$ versus X, similar to that shown in Fig. 1, for the 191 Sahara Desert data bins indicated $C_{SW} \approx 0.33$. Measured values of $R/\bar{R}$ are plotted in Fig. 2 as a function of γ for six $U - U_0$ bins which have large VV_0 values (i.e., small UU_0) and, thus, best illustrate azimuthal anisotropy. These data are well correlated along a representative curve generated by Eq. (6) with mean values of U and U_0 and $C_{SW} = 0.33$.

The azimuthal phase function, as related by Eq. (6), has several notable features. First, it will accommodate predominately backward-reflecting surfaces ($C_{SW} > 0$) such as the Sahara–Arabian Desert, predominately forward-reflecting surfaces ($C_{SW} < 0$), and isotropic surfaces ($C_{SW} = 0$). Second, azimuthal dependence is minimal if one or both of the zenith angles are near their nadirs ($VV_0 \approx 0$) which is a generally observed phenomenon. And third, the phase function exhibits zenith angle reciprocity which will be discussed in more detail later.

c. Gibson and Saudi directional models

Bidirectional reflectance parameters RUU_0 for the Gibson Desert are presented in Fig. 3 as a function of X (left scale). These data were taken during July 1979, when the noontime solar zenith angle was near its maximum yearly value ($\theta_0 \approx 50°$), and best illustrate the relatively high anisotropy of this target site. The back-reflecting data lie along the top dashed line, the fore-reflecting data lie along the bottom dashed line, and the side-reflecting data lie between. However, when normalized by the azimuthal phase function, $P_{SW}(C_{SW} = 0.60)$, these data collapse into a single line (right

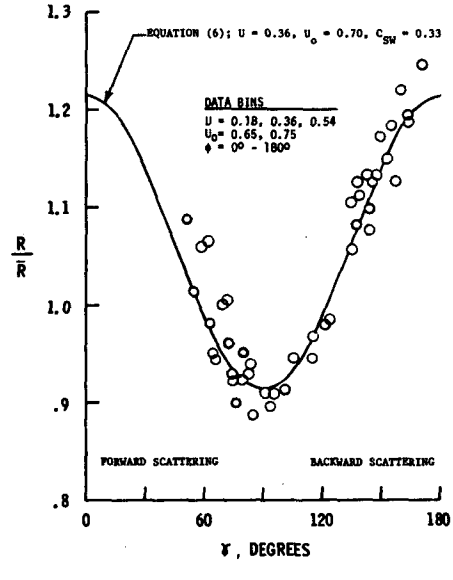

FIG. 2. Illustration of the Rayleigh-like shape of the azimuthal phase function as a function of scattering angle. Data from Sahara–Arabian Desert for high zenith angles.

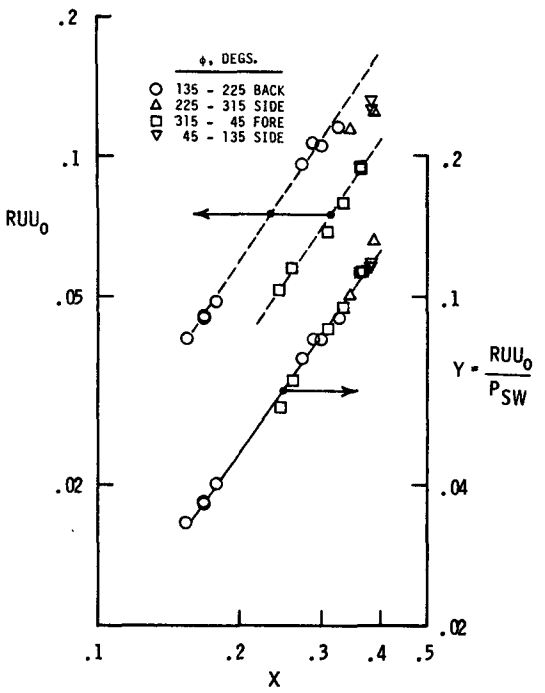

FIG. 3. Normalization of the bidirectional reflectance for the Gibson Desert site; $\theta_0 \approx 50°$, July 1979.

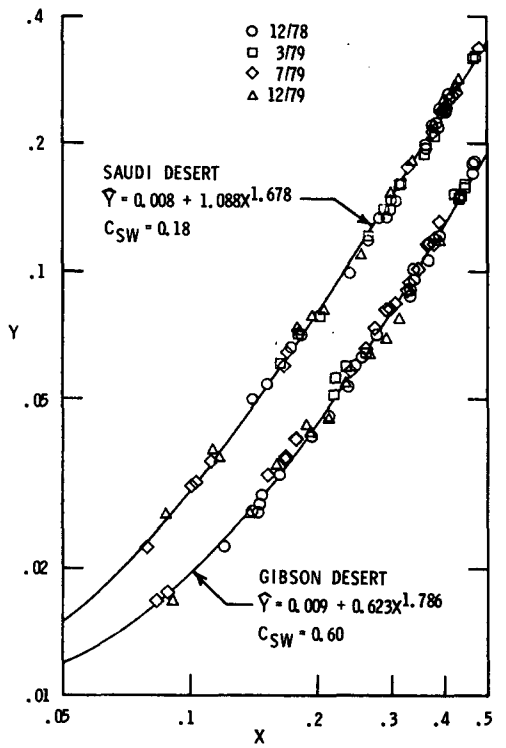

FIG. 4. As in Fig. 1 but for the Gibson and Saudi Desert sites.

scale). All of the normalized Gibson and Saudi (C_{SW} = 0.18) data for the four sampled months are given in Fig. 4 and are well correlated along regression curves related by Eq. (3). Regression coefficients used for the desert reflection models are listed in Table 3.

Anisotropic reflection diagrams (i.e., R/A) are given in Fig. 5 for the Gibson (left) and Saudi (right) Deserts. The diagrams show that both desert sites are predominately back-reflectors, for $U_0 = 0.6$, and that the Saudi Desert is more nearly isotropic.

d. Albedo

Local albedo can be expressed as

$$A = 2\int_0^1 \bar{R}UdU \tag{7}$$

which with the substitution of Eq. (3) becomes

$$A = 2Y_0U_0^{-1} + 2Y_1U_0^{N-1}\int_0^1 [U/(U+U_0)]^N dU. \tag{8}$$

The albedo curves given in Fig. 6 were computed from Eq. (8) with the coefficients listed in Table 3. Bin-integrated albedos for the Sahara–Arabian Desert (Taylor et al., 1983) are in good agreement with their computed curve. However, aircraft pyranometer (0.3–3.0 μm) measurements for the Saudi Desert (Davis and Cox, 1981) are considerably below ($\approx$85%) the computed albedos and indicate better agreement with the Sahara–Arabian values.

5. Emitted longwave

There was little variation of the emitted longwave radiances with azimuth angle for the Sahara–Arabian dataset, and the directional emittance defined as

$$\bar{L}_{LW} = \frac{1}{2\pi}\int_0^{2\pi} L_{LW}d\phi \tag{9}$$

was computed for all $\theta - \theta_0$ bins. Values of $\bar{L}_{LW}$ plotted in Fig. 7 versus secθ on a log-log scale are quite linear for each U_0 and can be related as a power-law of U as

$$\bar{L}_{LW,\theta} = \bar{L}_{LW,0°}(\sec\theta)^{-M} = \bar{L}_{LW,0°}U^M. \tag{10}$$

Staylor (1985) previously found that this limb-darkening function also applied for overcast clouds.

Initial attempts to model the L_{LW} data for the Gibson and Saudi Deserts in a similar manner were somewhat disappointing. For instance, the Gibson longwave ra-

TABLE 3. Reflection model coefficients.

Desert site	Y_0	Y_1	N	C_{SW}	$\sigma/\bar{Y}$
Sahara–Arabian	0.011	0.920	1.764	0.33	0.054
Gibson	0.009	0.623	1.786	0.60	0.077
Saudi	0.008	1.088	1.678	0.18	0.057

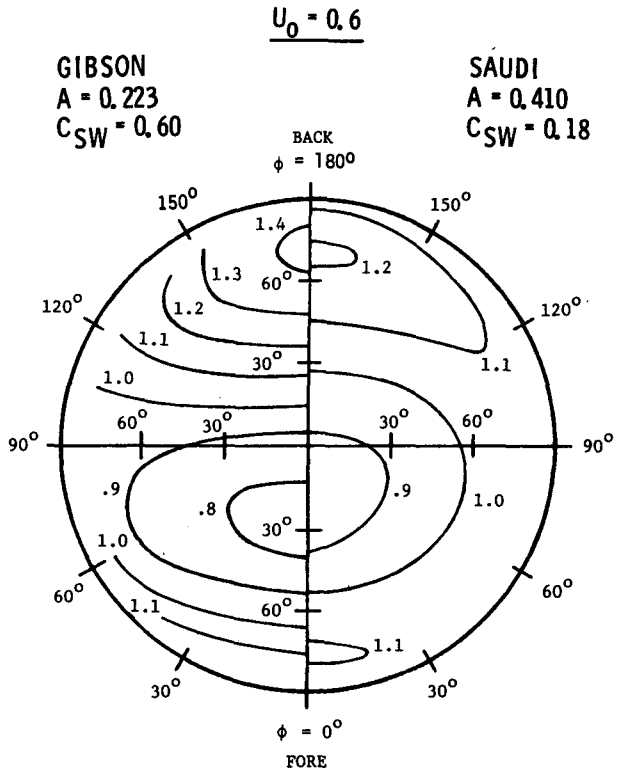

FIG. 5. Anisotropic reflectance diagrams computed from the Gibson and Saudi Desert models; $U_0 = 0.6$.

diances for July 1979 ($\theta_0 \approx 50°$) behaved, on a reduced scale, in a manner very similar to the shortwave reflectances shown in Fig. 3. Namely, the back-radiances ($\phi = 135°$ to $225°$) were higher and the fore-radiances

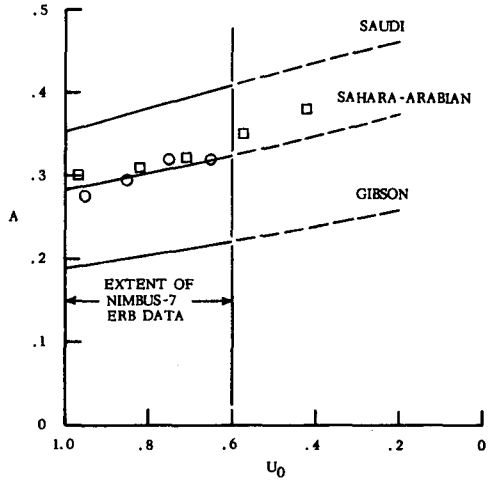

FIG. 6. Albedos computed from the Saudi, Sahara–Arabian and Gibson Desert models. Circular symbols are bin-integrated values for the Sahara–Arabian Desert from Taylor et al. (1983). Square symbols are measurements for the Saudi Desert from Davis and Cox (1981).

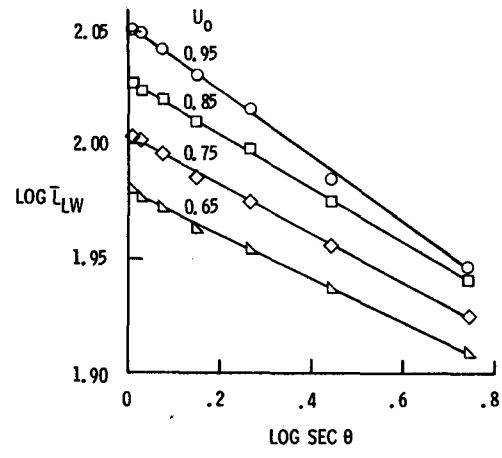

FIG. 7. Correlation of limb-darkening with zenith angle for the Sahara–Arabian Desert.

($\phi = 315°$ to $45°$) were lower than the mean values. It was found that this emission anisotropy could be removed, to a large degree, by an azimuthal phase function that was identical in form as that used for the shortwave:

$$P_{LW} = \frac{L_{LW}}{\bar{L}_{LW}} = \frac{1 + C_{LW}[UU_0 - VV_0 \cos\phi]^2}{1 + C_{LW}[(UU_0)^2 + \frac{1}{2}(VV_0)^2]}. \quad (11)$$

Normalized longwave radiances, L_{LW}/P_{LW}, presented in Fig. 8 for the Gibson and Saudi sites and for summer and winter conditions are generally linear even to quite large zenith angles. All regression coefficients and constants determined for the desert emissions models are listed in Table 4. The longwave radiant exitance expressed as

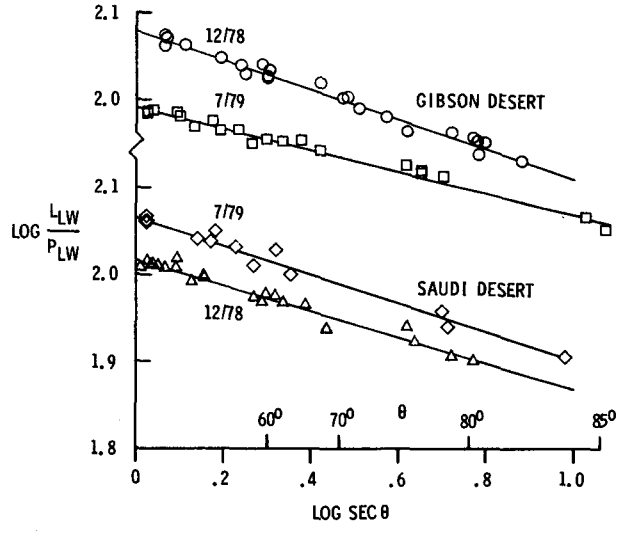

FIG. 8. As in Fig. 7 but for the Gibson and Saudi Desert sites. Note stepped vertical scales.

TABLE 4. Emission model parameters.

Desert site	Time period	U_0	C_{LW}	M	$\bar{L}_{LW,0°}$ (W m^{-2} sr^{-1})	E_{LW} (W m^{-2})
Sahara–Arabian	11/78 to 5/80	0.95	0.01	0.144	113	331
		0.85	0.01	0.117	107	317
		0.75	0.01	0.107	101	301
		0.65	0.01	0.095	95	285
Gibson	12/78	0.99	0.04	0.170	120	348
	7/79	0.65	0.04	0.121	98	290
Saudi	7/79	0.99	0.02	0.164	116	337
	12/78	0.72	0.02	0.148	104	304

$$E_{\mathrm{LW}} = \frac{2\pi}{2 + M} \bar{L}_{\mathrm{LW},0°} \tag{12}$$

can be computed from these values.

6. Discussion of results

a. *Reflected shortwave*

Comparisons of the December 1978 and December 1979 data for both the Gibson and Saudi Deserts (Fig. 4) indicate that there were no significant differences in the levels of the measurements. Therefore, it was assumed that the satellite sensor responses were constant during this period and during the somewhat longer period of the Sahara–Arabian dataset. Sensor stability is important, particularly for modeling purposes, in that a continuous degradation of the sensors during the December 1978 to July 1979 period, for instance, could have been erroneously incorporated into the models as a θ_0-effect.

The multi-axis ERB scanner obtained measurements for all azimuth angles; however, with the assumption of symmetry about the principal plane, the $\phi = 0°$ to 360° data were mapped into $\phi = 0°$ to 180° values for the binned, Sahara–Arabian dataset. Desert sand dunes are usually aligned with the prevailing winds, and this assumption might not be valid for such surfaces. Although the validity of the symmetry assumption could not be assessed for the Sahara–Arabian dataset, there were no significant differences between the $\phi = 0°$ to 180° and $\phi = 180°$ to 360° measurements for the Gibson and Saudi Deserts.

Error sources for the present modeled data include site nonuniformity, instrument noise, meteorological variations, and modeling errors. In spite of such potential errors, the model dispersions (standard deviation/mean) were only 5% to 8% (Table 3), and site nonuniformities alone could account for a major portion of these dispersions.

All zenith angle terms in the directional model, Eq. (3), and in the azimuthal phase function, Eq. (6), appear only in sum or product combinations (i.e., $U + U_0$, UU_0 and VV_0), and therefore, reciprocity exists between the viewing and solar zenith angles. (The values of θ and θ_0 can be switched and the value of R will be unchanged.) This feature of the target sites allows the present limited range of θ_0 values to be extended to the more extensive present range of θ values, and lends a degree of confidence to the U_0-extrapolation of the site albedos given in Fig. 6. The general form of the present model is probably applicable to most deserts and arid regions, and perhaps to other diffuse surfaces.

b. *Emitted longwave*

The longwave radiance model given by Eqs. (10) and (11) provided good estimates for the noontime Nimbus-7 ERB measurements, but its regression values, $L_{\mathrm{LW},0°}$ and M, apply only to noontime and not to other hours of the day. For instance, the noontime values of $L_{\mathrm{LW},0°}$ and E_{LW} are quite linear with U_0 for the Sahara–Arabian Desert (Table 4), yet these values are larger in the afternoon than in the morning for the same U_0 (Minnis and Harrison, 1984). Therefore, while the present longwave models offer a useful method for correlating longwave radiance measurements taken at a given time of day, they cannot be used to compute diurnal parameters in a manner similar to the shortwave models.

The azimuthal anisotropy for the longwave radiances came somewhat as a surprise. However, it should be expected that the side of sand dunes, rocks and other vertical protuberances facing toward the Sun would be somewhat warmer, and thus, would emit more energy in that direction than would the opposite side in its direction. These protuberances may also be the major cause of the shortwave anisotropy. (Note that the C_{LW} values given in Table 4 are an order-of-magnitude smaller than the C_{SW} values given in Table 3).

7. Summary

Broadband shortwave and longwave radiance measurements obtained from the Nimbus-7 ERB scanner were used to develop cloud-free reflectance and emittance models for the Sahara–Arabian, Gibson, and Saudi Deserts. The bidirectional reflectance model for these desert sites was a function of sum and product terms of cosine solar and viewing zenith angles and, thus, reciprocity existed between these zenith angles. This feature of the sites allows the present limited range of solar zenith angles to be modeled to the more extensive present range of viewing zenith angles. The emittance model was related by a power-law of cosine viewing zenith angle. The general forms of both the reflectance and emittance models are probably applicable to most deserts and arid regions, and perhaps to other diffuse surfaces.

REFERENCES

Barkstrom, B. R., 1973: A comparison of the Minneart reflectance law and the reflectance from a nonconservative isotropic scattering atmosphere. *J. Geophys. Res.*, **78,** 6370–6372.

Bryson, R. A., and D. A. Baerreis, 1967: Possibilities of major climatic modification and their implications: Northwest India. *Bull. Amer. Meteor. Soc.*, **48**(3), 136–142.

Davis, J. M., and S. K. Cox, 1981: Regional properties of angular reflectance Models. Atmos. Sci. Paper No. 338, Colorado State University, 126 pp.

Jacobowitz, H., H. V. Soule, H. L. Kyle, F. B. House and the Nimbus 7 ERB Experiment Team, 1984: The Earth Radiation Budget (ERB) Experiment: An Overview. *J. Geophys. Res.*, **89**(D4), 5021–5038.

Minnis, P., and E. F. Harrison, 1984: Diurnal variability of regional cloud and clear-sky radiative parameters derived from GOES data. Part I: Analysis Method. *J. Climate Appl. Meteor.*, **23,** 993–1011.

Short, N. M., P. D. Lowman, S. C. Freden and W. A. Finch, 1976: Mission to Earth: Landsat views the world, NASA SP-360.

Staylor, W. F., 1985: Reflection and emission models for clouds derived from Nimbus 7 ERB scanner measurements. *J. Geophys. Res.*, **90**(D5), 8075–8079.

Stowe, L. L., 1983: Validation of Nimbus 7 Temperature-humidity infrared radiometer (THIR) estimates of cloud type and amount. *Advances in Space Research,* **2,** 15–19.

——, and M. D. Fromm, 1983: Nimbus 7 ERB sub-target radiance tape (STRT) data base. NOAA TM NESDIS 3.

Taylor, V. R., and L. L. Stowe, 1984: Reflectance characteristics of uniform Earth and cloud surfaces derived from Nimbus-7 ERB. *J. Geophys. Res.*, **89**(D4), 4987–4996.

——, —— and J. M. Vilando, 1983: Nimbus 7 ERB reflectance models for ERBE processing. *Proc. Fifth Conf. on Atmospheric Radiation,* Baltimore, Amer. Meteor. Soc., 452–455.